RSC Advances

PAPER

View Article Online
View Journal | View Issue

Cite this: *RSC Adv.*, 2024, **14**, 24413

Magnetically recyclable spherical $Cu_2O@Fe_3O_4$ S-scheme heterojunction for efficient tetracycline removal *via* visible light-activated peroxydisulfate†

Jiahao Wang,[a] Lianyue Zhang,[a] Haiyue Zhang,[a] Runyu Cai,[a] Hengda Jin,[a] Man Xu,*[ac] Xuan Cao *[abd] and Shuhua Yao*[a]

Received 7th June 2024
Accepted 23rd July 2024

DOI: 10.1039/d4ra04174g

rsc.li/rsc-advances

The overuse of antibiotics in treating bacterial infections is a significant threat to the environment and human health. The utilization of visible-light-assisted peroxydisulfate (PDS) activation for eliminating organic pollutants is a promising approach. This study uses a straightforward hydrothermal method to prepare magnetically recyclable spherical $Cu_2O@Fe_3O_4$. The efficacy of this material in removing antibiotic pollutants was assessed using simulated wastewater containing tetracycline (TC). TC removal was achieved by activating PDS with $Cu_2O@Fe_3O_4$ as the visible light photocatalyst. Experimental findings revealed that under specific conditions—a pH of 9, a $Cu_2O@Fe_3O_4$ concentration of 60 mg L^{-1}, and a PDS concentration of 25 mg L^{-1}—the removal rate of TC reached 97.67% after 30 min of irradiation. Moreover, $Cu_2O@Fe_3O_4$ exhibited excellent recyclability, maintaining a removal rate of 93.33% after five recycling rounds. X-ray diffraction characterization of the $Cu_2O@Fe_3O_4$ composite before and after cycling confirmed its robust stability and reusability. *In situ* X-ray photoelectron spectroscopy analysis showed that electrons migrated from Fe_3O_4 to Cu_2O during the photocatalytic reaction, indicating the formation of an S-type heterojunction in $Cu_2O@Fe_3O_4$. Free radical trapping experiments demonstrated the active involvement of ·OH, $\cdot O_2^-$, $SO_4^{\cdot -}$ and h^+ radicals in TC removal.

Introduction

The initial oversight of antibiotics' environmental toxicity owing to their remarkable therapeutic effects led to their excessive use. Over time, this misuse has resulted in serious environmental issues. Tetracycline (TC), extensively employed in medical and livestock sectors, is a significant environmental and health threat owing to its overconsumption.[1] Its accumulation in ecosystems and subsequent impact on microbial communities exacerbates the proliferation of antibiotic resistance.[2] Moreover, TC jeopardizes the safety of potable and irrigation water, disrupting human intestinal flora and posing health risks to various organisms. These adverse effects have raised significant concerns about TC contamination, requiring urgent attention as a public health issue.[3] Consequently, there is a pressing need to develop efficient and cost-effective methods for TC degradation.

Various methods exist for removing antibiotics from wastewater, including adsorption treatment, biological treatment, and membrane processes.[4,5] Advanced oxidation processes (AOPs) are a promising technology for the partial or complete mineralization of pollutants through highly active free radicals such as hydroxyl radicals (·OH), sulfate radicals ($SO_4^{\cdot -}$), and superoxide radicals ($\cdot O_2^-$).[6] Among these, the peroxydisulfate activation process generates $SO_4^{\cdot -}$, which has a higher standard redox potential (E_0 = 2.5–3.1 V) compared to ·OH (E_0 = 1.89–2.72 V), thereby exhibiting strong oxidation capability.[7] Photo-assisted persulfate activation (PPA) is gaining significant attention owing to its environmental friendliness, sustainability, and excellent chemical stability. PPA is widely employed to degrade antibiotics in aquatic environments.

Photocatalysis is a novel and environmentally friendly advanced oxidation technology.[8] For photocatalysts to be highly effective, they must have abundant active sites, broad spectral absorption, rapid separation and migration rates of photogenerated electrons and holes, and robust oxidation and reduction capabilities.[9] Among these factors, the construction of heterogeneous junctions by combining semiconductors is recognized as one of the most promising approaches for achieving photocatalytic electron–hole separation through the electric field formed by the heterojunction.[10] Heterogeneous photocatalysts exhibit distinct mechanisms for photogenerated carrier transfer, stemming from variations in preparation

[a]*Shenyang University of Chemical Technology, Shenyang 110142, Liaoning, China*
[b]*School of Engineering, Westlake University, Hangzhou 310024, China*
[c]*Instrumental Analysis Center, Shenyang University of Chemical Technology, Shenyang 110142, China*
[d]*Center for Interdisciplinary Research and Innovation, Muyuan Laboratory, Zhengzhou, Henan 450016, China*

† Electronic supplementary information (ESI) available. See DOI: https://doi.org/10.1039/d4ra04174g

methods, energy bands, morphologies, and structures. Based on the diverse mechanisms of photogenerated carrier transfer, heterogeneous photocatalysts are generally categorized into I-, II-, Schottky-, Z-, and S-types.[11] S-Type heterogeneous photocatalysts garner significant attention owing to their unique advantages.[12,13] In S-type heterogeneous photocatalytic systems, incorporating internal built-in electric fields (IEFs) effectively regulates the direction of carrier migration, enhancing the oxidation and reduction capabilities and extending the lifetimes of photogenerated holes and electrons. Thus, establishing S-type heterogeneous junctions is an effective strategy for enhancing photocatalytic efficiency.

Thus far, cuprous oxide (Cu_2O) has exhibited remarkable photocatalytic performance, boasting a band gap width aligning with the visible light wavelength range, rendering it directly excitable by solar light.[14] However, its instability arises from a tendency to undergo an irreversible redox disproportionation reaction.[15] On the other hand, magnetite (Fe_3O_4) demonstrates photocatalytic capabilities and possesses considerable magnetic properties, facilitating easy separation and recovery from the reaction system, resulting in its widespread adoption in photocatalysis.[16] Khaled Benabbas *et al.* Employed a hydrothermal approach to fabricate a magnetically separable Fe_3O_4/CuO composite core–shell heterostructure photocatalyst. Fe_3O_4/CuO displayed remarkable optical characteristics, including a low band gap value and superior light absorption capabilities. Evaluation of its photocatalytic activity in DR89 removal under visible light irradiation showcased the superior performance of the Fe_3O_4/CuO composite, surpassing pure CuO and Fe_3O_4 by 11 and 8 times, respectively. Similarly, Alani *et al.* used the hydrothermal method to produce a visible-light-driven biotemplated magnetic copper oxide (CuO/C/Fe_3O_4) photocatalyst. They found that CuO/C/Fe_3O_4 outperformed spherical polyhedral Fe_3O_4 NPs in catalytic activity. Visible light exposure of the CuO/C/Fe_3O_4 photocatalyst increased the generation of hydroxyl radicals ($\cdot OH$), superoxide anion radicals ($\cdot O_2^-$), and the redox Fe^{3+}/Fe^{2+} pair, thereby enhancing photodegradation performance.

In this study, we synthesized a magnetic $Cu_2O@Fe_3O_4$ composite material *via* a thermal precipitation method. *In situ* X-ray photoelectron spectroscopy analysis showed that electrons migrated from Fe_3O_4 to Cu_2O during the photocatalytic reaction, indicating the formation of an S-type heterojunction in $Cu_2O@Fe_3O_4$. A comprehensive structural analysis of $Cu_2O@Fe_3O_4$ was conducted utilizing scanning electron microscopy, X-ray diffraction techniques, and energy-dispersive X-ray spectroscopy. Additionally, we confirmed its magnetic nature and strong magnetic properties. Furthermore, we elucidated the optical absorption spectrum of $Cu_2O@Fe_3O_4$ through UV-visible diffuse reflection spectroscopy. To assess the practical utility of the composite material, we employed a TC solution to simulate antibiotic wastewater. We applied the $Cu_2O@Fe_3O_4$ composite material with sodium persulfate for efficient degradation. Under illumination, photogenerated electrons facilitate the *in situ* redox cycling of Cu(II)/Cu(I) in $Cu_2O@Fe_3O_4$, significantly enhancing the activation efficiency of PDS and yielding more sulfate radicals ($SO_4^{\cdot -}$). Through this experimentation, we investigated the degradation mechanism and influential factors associated with the composite material, thus experimentally validating its potential for application in antibiotic wastewater treatment.

Materials and methods

Reagents

Ferrous sulfate heptahydrate ($FeSO_4 \cdot 7H_2O$), hydrochloric acid (HCl), sodium molybdate dihydrate ($Na_2MoO_4 \cdot 2H_2O$), disodium ethylenediaminetetraacetate (EDTA-2Na), sodium hydroxide (NaOH), isopropanol (C_3H_8O, IPA), copper nitrate trihydrate ($Cu(NO_3)_2 \cdot 3H_2O$), L-ascorbic acid (ASA), ethylene glycol ($C_2H_6O_2$), ethanol (C_2H_5OH), tetracycline (TC), sodium persulfate ($Na_2S_2O_8$) were purchased from China Pharmaceutical Group. In addition, all solutions were prepared using distilled water.

Synthesis of Fe_3O_4

The hydrothermal method was utilized to synthesize Fe_3O_4 by introducing ferrous sulfate ($FeSO_4$) as a starter material. Briefy described, 0.278 g (1 mmol) ferrous sulfate heptahydrate ($FeSO_4 \cdot 7H_2O$) and 0.242 g (1 mmol) sodium molybdate dihydrate ($Na_2MoO_4 \cdot 2H_2O$) were dissolved in a 15 mL distilled water, respectively. After complete dissolution, the $FeSO_4$ solution was transferred into the Na_2MoO_4 solution, and pH to 9 was adjusted with NaOH solution. Subsequently, the mixture was transferred into a 50 mL Tefonlined autoclave, sealed, and heated for 24 h at 180 °C followed by cooling naturally. After that, the formed precipitate was recovered by applying a magnetic field with an external magnet in order to be washed with distilled water and ethanol; once washed, the prepared catalyst was put to dry at 60 °C for 12 h and the obtained product was labelled as Fe_3O_4.

Synthesis of $Cu_2O@Fe_3O_4$ composite

0.2416 g (1 mmol) of copper nitrate trihydrate ($Cu(NO_3)_2 \cdot 3H_2O$) were dissolved in 8.5 mL of ethylene glycol ($C_2H_6O_2$) and 17 mL of ethanol (C_2H_5OH); after being stirred for 30 min; add 25 mg of iron oxide in the medium. Subsequently, the samples were placed in an ultrasonic cleaner for 30 minutes. After that, the mixture was transferred into a 50 mL Tefonlined autoclave, sealed, and heated for 5 h at 160 °C followed by cooling naturally. After that, it was washed several times with distilled water and ethanol and finally was put to dry at 60 °C for 24 h and the obtained product was labelled as $Cu_2O@Fe_3O_4$.

Characterizations

The powder X-ray diffraction (XRD) measurements were performed using a D8 Advance Bruker X-ray diffractometer, utilizing Cu Kα radiation ($\lambda = 0.5418$ nm) under conditions of 56 kV and 182 mA. The diffraction data were collected over a range of 15° to 80° (2θ) at room temperature. To observe morphology and perform element mapping analysis, a scanning electron microscope (SEM-JSM-6360LV) equipped with energy dispersive X-ray spectroscopy (EDX-S-3400N) was

utilized. The chemical composition and valence states of the samples were analyzed using X-ray Photoelectron Spectroscopy (XPS-Thermo ESCALAB 250), with further investigation into the charge transfer pathway. Additionally, the spectra were calibrated relative to the C1s peak at 284.8 eV. The magnetic characteristics of the samples were investigated utilizing the Quantum Design-PPMS system. The optical adsorption capacity of the catalysts was assessed using the Hitachi U4100 UV spectrometer, operating within the spectral range of 190–900 nm. Transient photocurrent and electrochemical impedance were investigated using an electrochemical workstation (CHI 852C, Germany). Photoluminescence (PL) spectra were obtained using a HORIBA spectrometer, with a monochromator slit width of 5.0 nm.

Photocatalytic activity investigations

The performance of the $Cu_2O@Fe_3O_4$/PDS/Vis system was evaluated by assessing the removal rate of tetracycline (TC) from aqueous solutions. Experiments were conducted using TC concentrations ranging from 10 to 40 mg L^{-1} in a total volume of 200 mL. Reactions were carried out in a 250 mL reaction vessel equipped with a metal halide lamp as the visible light source. To establish suitable reaction conditions, the pH of the system was adjusted between 3.0 and 11.0 using HCl and NaOH. The catalyst, $Cu_2O@Fe_3O_4$, was dosed within the range of 0.02 to 0.1 g L^{-1} and mixed into the 200 mL TC solution. Subsequently, a specific dosage of PDS, ranging from 0.015 to 0.045 g L^{-1}, was added to activate the photocatalytic process. Samples were collected every five minutes and filtered through a 0.22 μm filter membrane to obtain a clear liquid suitable for analysis. The concentration of TC was determined using a UV-Vis spectrophotometer (MAPADA, UV-1800PC) at a wavelength of 355 nm. The removal efficiency of TC was calculated using the following equation:

$$\text{Removal efficiency} = \left(1 - \frac{C_t}{C_0}\right) \times 100\%$$

where C_0 represents the initial concentration of TC, and C_t represents the concentration of TC at a given time.

Results and discussion

Characteristics of $Cu_2O@Fe_3O_4$

The X-ray diffraction (XRD) patterns of Fe_3O_4 and $Cu_2O@Fe_3O_4$ materials are shown in Fig. 1(a) and (b). Fig. 1(a) displays distinct characteristic peaks, with observed peaks at 2θ values of 18.3°, 30.1°, 35.4°, 37.1°, 43.1°, 53.4°, 56.9°, 62.5°, 65.7°, 70.9°, 74°, 75°, and 78.9°, precisely matching the peak positions and intensities of Fe_3O_4 (PDF#76-1849). These peaks correspond to the crystallographic planes (111), (220), (311), (222), (400), (331), (422), (511), (440), (531), (620), (533), and (444) of Fe_3O_4, revealing a face-centered cubic crystal structure with space group $Fd\bar{3}m$ (No. 227). Similarly, Fig. 1(b) exhibits characteristic peaks, with observed peaks at 2θ values of 18.3°, 30.1°, 35.4°, 37.1°, 43.1°, 53.4°, 56.9°, 62.5°, 65.7°, 70.9°, 74°, 75°, and 78.9° (marked as '◆'), aligning perfectly with Fe_3O_4 (PDF#99-0073). These peaks correspond to crystallographic planes (111), (220), (311), (222), (400), (331), (422), (511), (440), (531), (620), (533), and (444), indicating a face-centered cubic crystal structure. Moreover, peaks marked as "●" at 2θ values of 29.6°, 36.4°, 42.3°, 52.5°, 61.3°, 69.6°, 73.5°, and 77.4° are confidently assigned to diffraction peaks of cubic-phase Cu_2O nanoparticles, corresponding to crystal planes (110), (111), (200), (211), (220), (310), (311), and (222) of Cu_2O (PDF#99-0041), with a face-centered cubic crystal structure and space group $Fd\bar{3}m$ (No. 224). Based on XRD data analysis, it can be preliminarily concluded that the synthesized sample corresponds to the desired $Cu_2O@Fe_3O_4$ composite material, confirming the successful implementation of the employed methodology.

For further analysis of the chemical composition and states of $Cu_2O@Fe_3O_4$, X-ray photoelectron spectroscopy (XPS) was employed, with results presented in Fig. 2. Fig. 2(a) provides the XPS spectra, where distinct peaks for O1s, Fe2p, Cu2p, CuLM2, and other species are observed. In Fig. 2(b), the XPS spectrum of iron in the composite material is depicted, revealing binding energies of $Fe2p_{1/2}$ and $Fe2p_{2/3}$ orbitals at 722.93 and 709.23 eV, respectively, consistent with literature data for Fe_3O_4.[17] Fig. 2(c) presents the energy spectrum of Cu2p in $Cu_2O@Fe_3O_4$, showing $Cu2p_{3/2}$ and $Cu2p_{2/3}$ orbitals at 931.5 and 951.33 eV, respectively, with a 19.83 eV difference. The absence of significant satellite peaks between them suggests the presence of Cu_2O in the prepared samples.[18] As depicted in Fig. 2(d), the composite sample exhibits two distinct peaks in the 1s orbital of oxygen, with binding energies of 528.92 and 530.19 eV, corresponding to lattice oxygen and oxygen molecules adsorbed on Cu_2O.[19] These XPS results further corroborate the predominance of Fe_3O_4 and Cu_2O in the processed samples.

Low-magnification scanning electron microscopy (SEM) images of the $Cu_2O@Fe_3O_4$ nanoparticles are depicted in Fig. 3(a), showcasing spherical particles with a uniform size distribution, predominantly ranging from 1000 to 1800 nm. Further high-magnification observations (Fig. 3(b) and (c)) show that the composite particles comprise numerous smaller nanoparticles, resembling the reported Cu_2O shell structure. The fabricated composite's surface composition and element distribution were quantitatively analyzed using energy-dispersive X-ray spectroscopy (EDS) techniques. Fig. 3(c)–(e) clearly show the uniform distribution of Cu, O, and Fe elements. Fig. 3(f) provides the atomic content of each element, indicating that Cu, O, and Fe constitute 17.81%, 13.12%, and 4.34%, respectively. Based on preliminary estimation, the Fe_3O_4 to Cu_2O ratio is determined to be 1 : 3. The SEM-EDS spectrum further confirms the successful synthesis of composites incorporating Fe_3O_4 and Cu_2O.

Through vibrating-sample magnetometer analysis, magnetic measurements and studies were conducted on the $Cu_2O@Fe_3O_4$ composite material. As depicted in Fig. 4, the composite material exhibits distinctive magnetic hysteresis loop characteristics. With the gradual increase of magnetic field strength, the material's magnetization increases, saturating at a magnetic field strength of approximately 1500 Oe. Analysis of Fig. 4 reveals the composite material's paramagnetic properties, with a residual magnetization of 2.7 emu g^{-1}, a coercivity

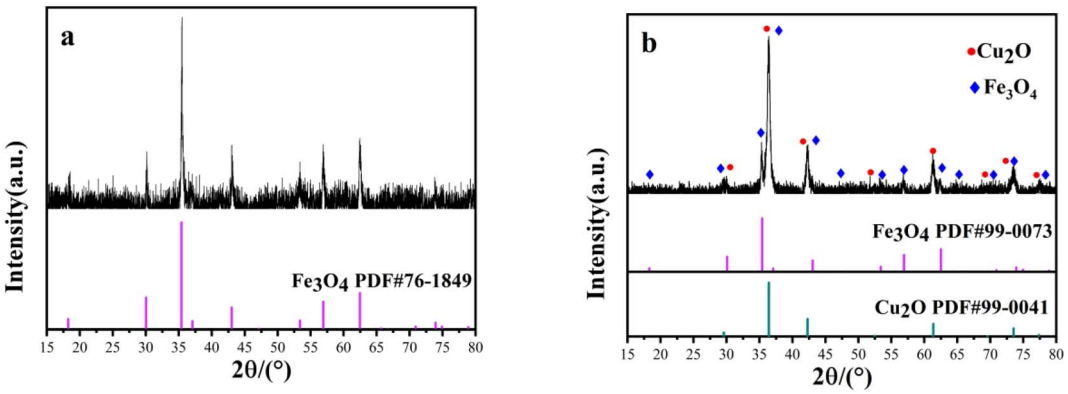

Fig. 1 (a) XRD patterns of Fe_3O_4 and (b) $Cu_2O@Fe_3O_4$.

measurement of 95.7 Oe, and a saturation magnetization of 10.4 emu g^{-1}. These characteristics underscore the composite material's high magnetic responsiveness and potential for separation and recovery, facilitating material recycling and reuse.

UV-Vis spectroscopy experiments were used to investigate the optical response of $Cu_2O@Fe_3O_4$ composite materials. As Fig. 5(a) shows, $Cu_2O@Fe_3O_4$ composite materials exhibited outstanding optical response. The composite materials demonstrated superior light absorption in the spectral range from 300 to 500 nm compared to pure Fe_3O_4. Employing the Kubelka–Munk relaxation function and UV-Vis spectroscopy, the energy gap of $Cu_2O@Fe_3O_4$ was estimated to be 1.74 eV, which is lower than that of Fe_3O_4 (2.12 eV). Literature reports suggest that a reduction in the energy gap can expand the light absorption range, consequently enhancing photon absorption and the generation of photogenerated carriers. This ultimately results in improved utilization efficiency of visible light during photocatalytic processes.[20]

We employed photoluminescence spectra (PL), intermittent transient photocurrent response spectra, and electrochemical impedance spectroscopy (EIS) for a comprehensive

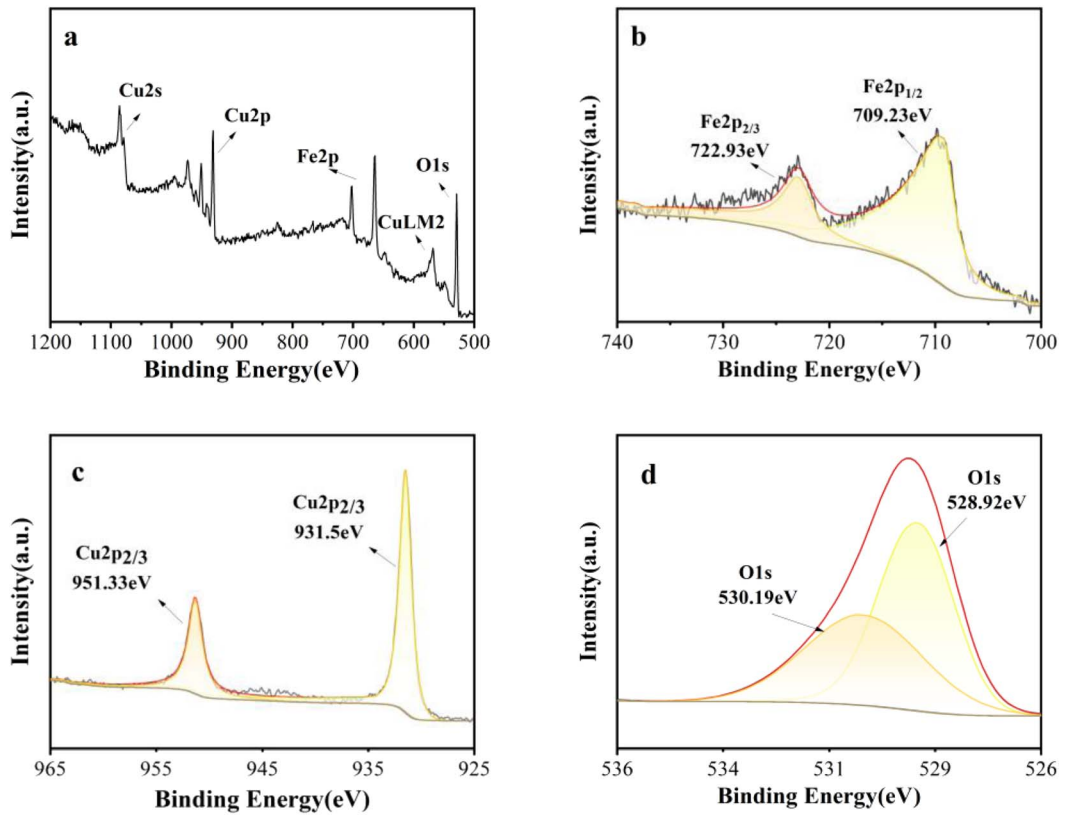

Fig. 2 (a) XPS patterns of $Cu_2O@Fe_3O_4$ survey, (b) Fe2p, (c) Cu2p, (d) O1s.

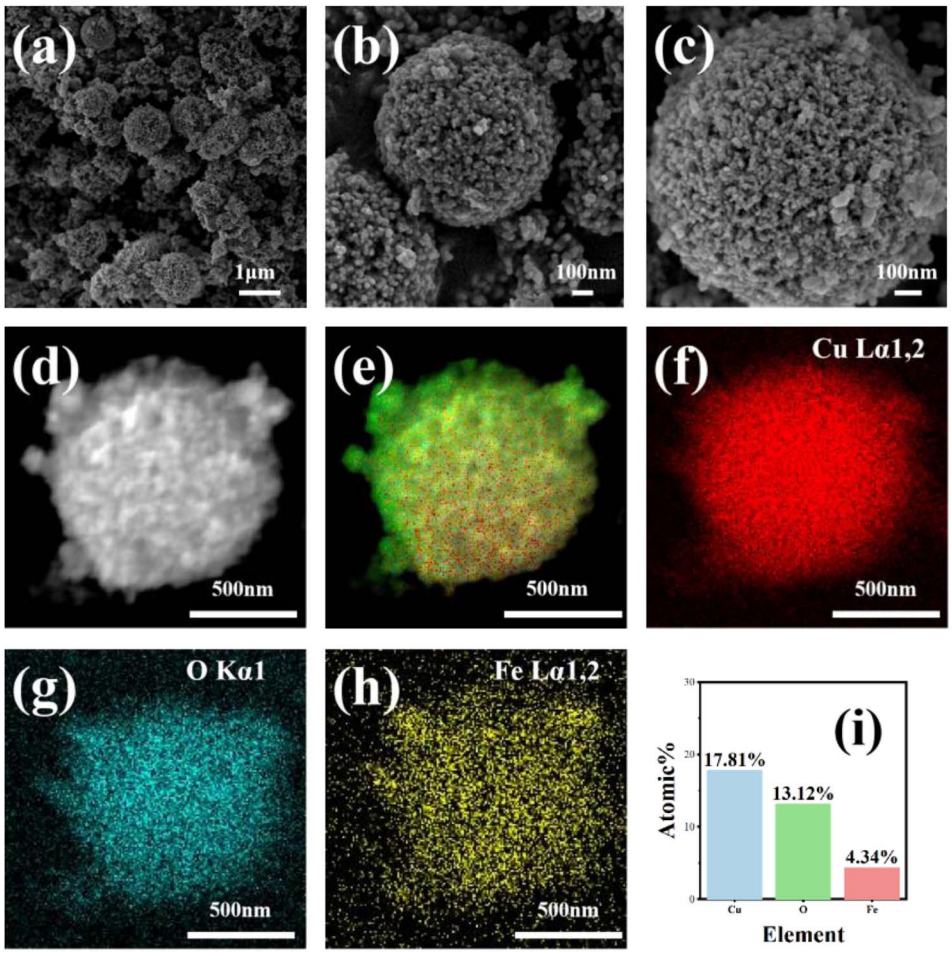

Fig. 3 (a)–(c) SEM images of $Cu_2O@Fe_3O_4$; (d) SEM images; (e) EDS full spectrum; (f)–(h) single element distribution map: (f) Cu; (g) Fe; (h) O; (i) the atomic content of Cu, O, and Fe.

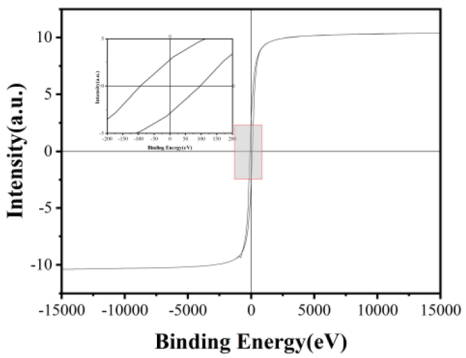

Fig. 4 The hysteresis loop of the $Cu_2O@Fe_3O_4$.

understanding of photo-electrochemical carrier separation. Fig. 6(a) clearly illustrates that the photoluminescence spectra (PL) intensity of $Cu_2O@Fe_3O_4$ is significantly lower compared to Fe_3O_4, indicating effective separation of photo-induced electrons and holes in the composite material.[21] The photocurrent response of $Cu_2O@Fe_3O_4$, as shown in Fig. 6(b), is nearly four times higher than that of Fe_3O_4. This intensified photocurrent enhances the separation of electrons and holes. Fig. 6(c) compares the EIS of $Cu_2O@Fe_3O_4$ and Fe_3O_4, revealing that $Cu_2O@Fe_3O_4$ exhibits a smaller arc radius than Fe_3O_4, facilitating the transfer of photogenerated carriers. The above-mentioned results further improve the successful construction of $Cu_2O@Fe_3O_4$ to avoid the combination of photo-induced electrons and holes. Therefore, this further confirms that $Cu_2O@Fe_3O_4$ possesses superior photocatalytic performance compared to pure Fe_3O_4. The degradation effect of tetracycline was studied by $Cu_2O@Fe_3O_4$ and Cu_2O under light, and the results are shown in Fig. S2.† Found that $Cu_2O@Fe_3O_4$ was superior to Cu_2O in its degradation activity. Please watch the ESI† for detailed data.

Effect of operational factors

Various reaction systems were established to investigate the removal rate of TC under different conditions. According to the calculation results illustrated in Fig. 7(a), it is evident that the removal rate under visible light conditions significantly surpasses that under dark conditions. In the presence of visible light, PDS is activated, leading to the degradation of TC (62.33%). Furthermore, $Cu_2O@Fe_3O_4$ exhibits activation under

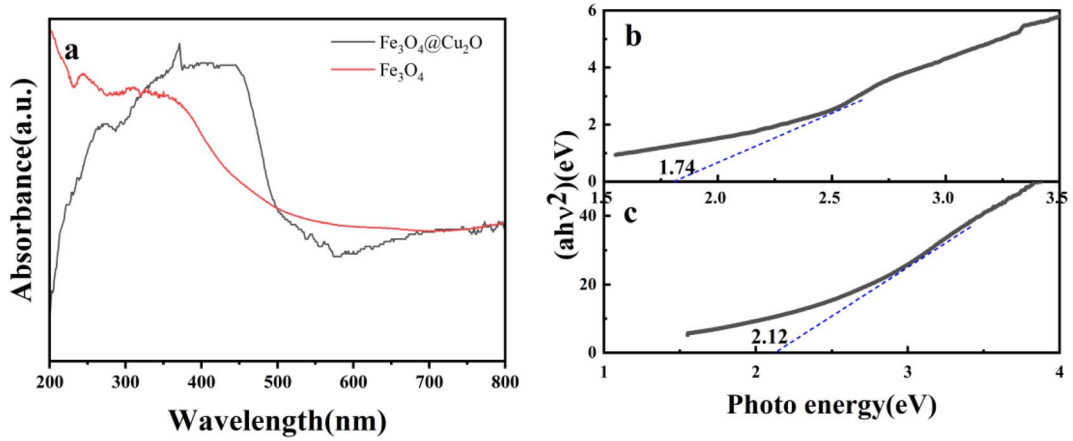

Fig. 5 (a) UV-Vis diffuse reflectance spectra of Cu_2O@Fe_3O_4 and Fe_3O_4, (b) $(\alpha h\nu)^2$ and $h\nu$ curves of Fe_3O_4@Cu_2O samples, (c) $(\alpha h\nu)^2$ and $h\nu$ curves of Fe_3O_4 samples.

visible light (81.86%), while Cu_2O@Fe_3O_4/PDS achieves the highest removal rate (97.67%) because both Cu_2O@Fe_3O_4 and PDS are activated synergistically.

The impact of Cu_2O@Fe_3O_4 dosage (20, 40, 60, 80, and 100 mg L^{-1}) on the removal efficiency of TC was thoroughly examined. As depicted in Fig. 7(b), with the gradual increase in Cu_2O@Fe_3O_4 dosage from 20 to 60 mg L^{-1}, the removal rate of TC increases from 89.3% to 97.6%. However, upon further increasing the dosage to 80 mg L^{-1}, the removal rate declines, dropping to 92.7%. Subsequently, at a dosage of 100 mg L^{-1}, the removal rate rebounds to 93.9%. These findings suggest that the optimal Cu_2O@Fe_3O_4 dosage for photocatalysis is 60 mg L^{-1}. At lower concentrations, increasing the catalyst dosage enhances the removal efficiency of TC. However, when the dosage surpasses a certain threshold (*e.g.*, from 60 to 100 mg L^{-1}), the removal rate of TC decreases owing to light scattering, which reduces light absorption within the reaction system.

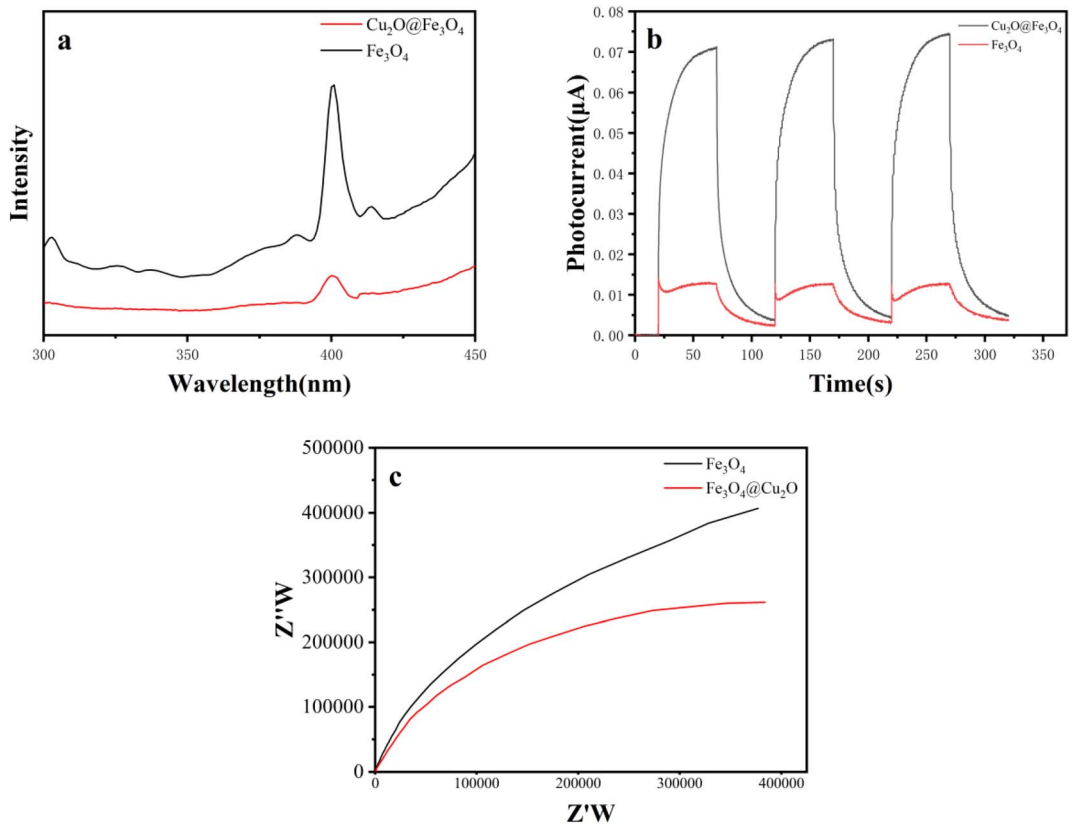

Fig. 6 (a) Photoluminescence spectra, (b) intermittent transient photocurrent response spectra, and (c) electrochemical impedance.

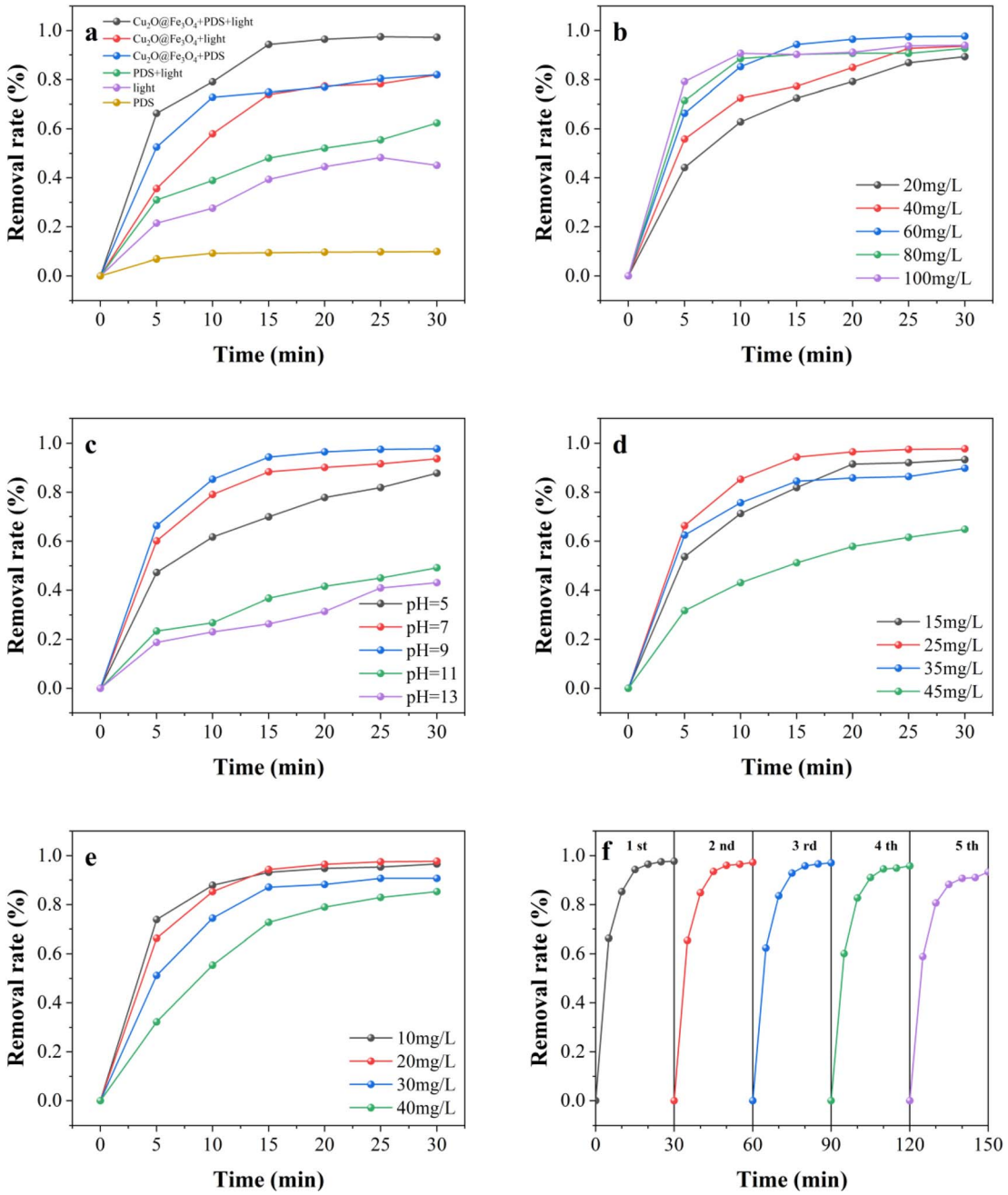

Fig. 7 (a) Comparison of the different reaction systems; (b) effect of $Cu_2O@Fe_3O_4$ dosage on TC removal performance; (c) effect of pH on TC removal performance; (d) effect of PDS dosage on TC removal performance; (e) effect of the initial TC concentration on TC removal performance; (f) recyclability and stability of the catalyst.

The initial pH of the solution plays a crucial role in TC removal. Thus, we investigated the impact of various pH values (5, 7, 9, 11, and 13) on the removal rate of TC under conditions of TC concentration at 20 mg L^{-1} and PDS concentration at 25 mg L^{-1}. The outcomes of these experiments are presented in Fig. 7(c). Increasing the solution's initial pH from 3 to 9 led to a slight increase in the rate of pollutant elimination, albeit not significantly. However, when the pH increased from 9 to 11, the removal efficiency of TC by $Cu_2O@Fe_3O_4$ composites considerably decreased from 97.6% to 43.1%. This decline indicates a decrease in the removal effectiveness of $Cu_2O@Fe_3O_4$ composites at higher pH values. Such an effect may be attributed to the decelerated rate of chemical reactions or the onset of competing reactions under high pH conditions, thereby impeding the degradation process to some extent.

The impact of PDS dosage on TC removal was investigated, with the corresponding data presented in Fig. 7(d). The experiment was conducted at room temperature, utilizing a $Cu_2O@Fe_3O_4$ dosage of 60 mg L^{-1} and a pH of 9. After 30 min, it was observed that within the range of 15–25 mmol L^{-1}, the removal

rate of TC exhibited an upward trend with increasing PDS concentration. This phenomenon can be attributed to the activation of PDS by photogenerated electrons or other free radical groups on the surface of $Cu_2O@Fe_3O_4$, thereby enhancing TC removal capability. However, beyond a PDS concentration of 25 mg L^{-1}, the removal rate of TC sharply declines. This decline may be attributed to potential competition that interferes with TC removal.

Various concentrations of TC (10, 20, 30, and 40 mg L^{-1}) were examined to evaluate their influence on the removal rate under different initial TC concentrations. Fig. 7(e) illustrates that, at room temperature, with a $Cu_2O@Fe_3O_4$ dosage of 60 mg L^{-1}, a solution pH of 9, and a PDS dosage of 25 mg L^{-1}, the initial TC concentration affects its removal rate. As the initial TC concentration increases from 10 to 20 mg L^{-1}, the removal rate gradually increases from 96.5% to 97.6%. However, upon further increasing the initial TC concentration to 90 mg L^{-1}, the removal rate declines to 20 mg L^{-1}. The increased TC concentration makes the wastewater deficient in sufficient radical oxidation, significantly reducing the removal rate.

To assess the stability of $Cu_2O@Fe_3O_4$, five cyclic reaction experiments were conducted under optimal conditions (room temperature, initial pH 9, TC dosage of 20 mg L^{-1}, $Cu_2O@Fe_3O_4$ composite catalyst dosage of 60 mg L^{-1}, and PDS dosage of 25 mg L^{-1}). The reacted $Cu_2O@Fe_3O_4$ composite material was collected using a magnet, washed, dried, and reused for subsequent cycles. As depicted in Fig. 7(f), the TC removal rates for the five cyclic experiments were 97.6%, 97.2%, 97%, 95.8%, and 93.3%, respectively. These results indicate a gradual decrease in the TC removal efficiency of the $Cu_2O@Fe_3O_4$ composite catalyst with increasing cycles. From the first to the fifth cycle, the TC removal rate consistently declined, suggesting a possible loss or deactivation of the catalyst's activity. This decline could be attributed to the blockage or damage of active sites on the catalyst surface, leading to reduced catalytic performance.

Complex XRD contrast after five cycling reactions

The $Cu_2O@Fe_3O_4$ composite underwent five cycles, with XRD performed before and after each cycle. Fig. 8 compares the XRD patterns of the composite before and after five reaction cycles. It was noted that the main diffraction peaks of the composite remained largely unchanged before and after cycling, indicating sustained stability in the crystal structure of the composite throughout the cycling process. However, there was a noticeable decrease in the intensity of each peak, suggesting that the cycling reactions might have reduced the material's phase purity.

In situ X-ray photoelectron spectroscopy analysis

Fig. 9(a) compares the XPS spectra before and after illumination, revealing distinct peaks for O1p, Fe2p, Cu2p, CuLM2, and other species. Fig. 9(b)–(e) depict the XPS spectra of $Cu_2O@Fe_3O_4$ before and after illumination, demonstrating shifts in the peaks corresponding to O1s, Fe2p, Cu2p, and CuLM2. Upon

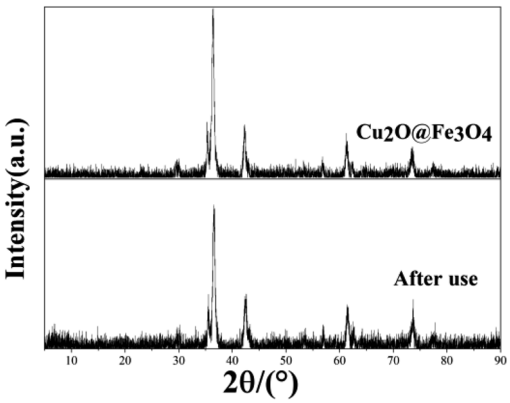

Fig. 8 XRD patterns of $Cu_2O@Fe_3O_4$ contrast after five cycling reactions.

illumination, the binding energy of $Fe2p_{1/2}$ and $Fe2p_{2/3}$ increased by 0.08 and 0.37 eV, respectively, indicating a decrease in the electron density of Fe_3O_4. Conversely, the binding energy of $Cu2p_{2/3}$ and $Cu2p_{3/2}$ decreased by 0.11 and 0.14 eV, respectively, indicating an increase in the electron density of Cu_2O.[22] These observations suggest the transfer of electrons from Fe_3O_4 to Cu_2O.

Free radical capture experiments

Previous studies have identified hydroxyl radical ($\cdot OH$), superoxide radical ($\cdot O_2^-$), holes (h^+), and sulfate radical ($SO_4^{\cdot -}$) as the radicals present in the AOP system. To identify the specific free radicals responsible for oxidizing TC in wastewater during our experiments, scavengers including acetylsalicylic acid (ASA), isopropanol (IPA), disodium ethylenediaminetetraacetate (EDTA-2Na), and ethanol (EtOH) were introduced to target $\cdot O_2^-$, $\cdot OH$, h^+, and $SO_4^{\cdot -}$, respectively. The results of these experiments are depicted in Fig. 10. Upon the addition of EDTA-2Na, ASA, IPA, and EtOH, the removal rate of TC decreased to 34.88%, 37.98%, 59.84%, or 86.82%, respectively. Hence, there is clear evidence that h^+, $\cdot O_2^-$, $SO_4^{\cdot -}$ and $\cdot OH$ play pivotal roles in the photocatalytic activation of sodium persulfate for TC removal.

Mechanistic analysis

According to the literature, Cu_2O and Fe_3O_4 exhibit distinct energy levels for their conduction and valence bands. Cu_2O features a conduction band at −1.2 eV and a valence band at 0.8 eV,[23] whereas Fe_3O_4 showcases a conduction band at 0.48 eV and a valence band at 2.08 eV.[24] When Cu_2O and Fe_3O_4 come into close contact under illumination, significant chemical interactions and charge redistribution at the interface facilitate electron transfer from Cu_2O to Fe_3O_4 (Fig. 11). This process generates an internal electric field (IEF) between the positively charged Cu_2O and negatively charged Fe_3O_4, accompanied by band bending. The combined effect of IEF and band bending excites Cu_2O and Fe_3O_4, prompting photogenerated electrons to migrate from the conduction band of Fe_3O_4 to the valence band of Cu_2O, where they recombine with holes. This photocatalytic

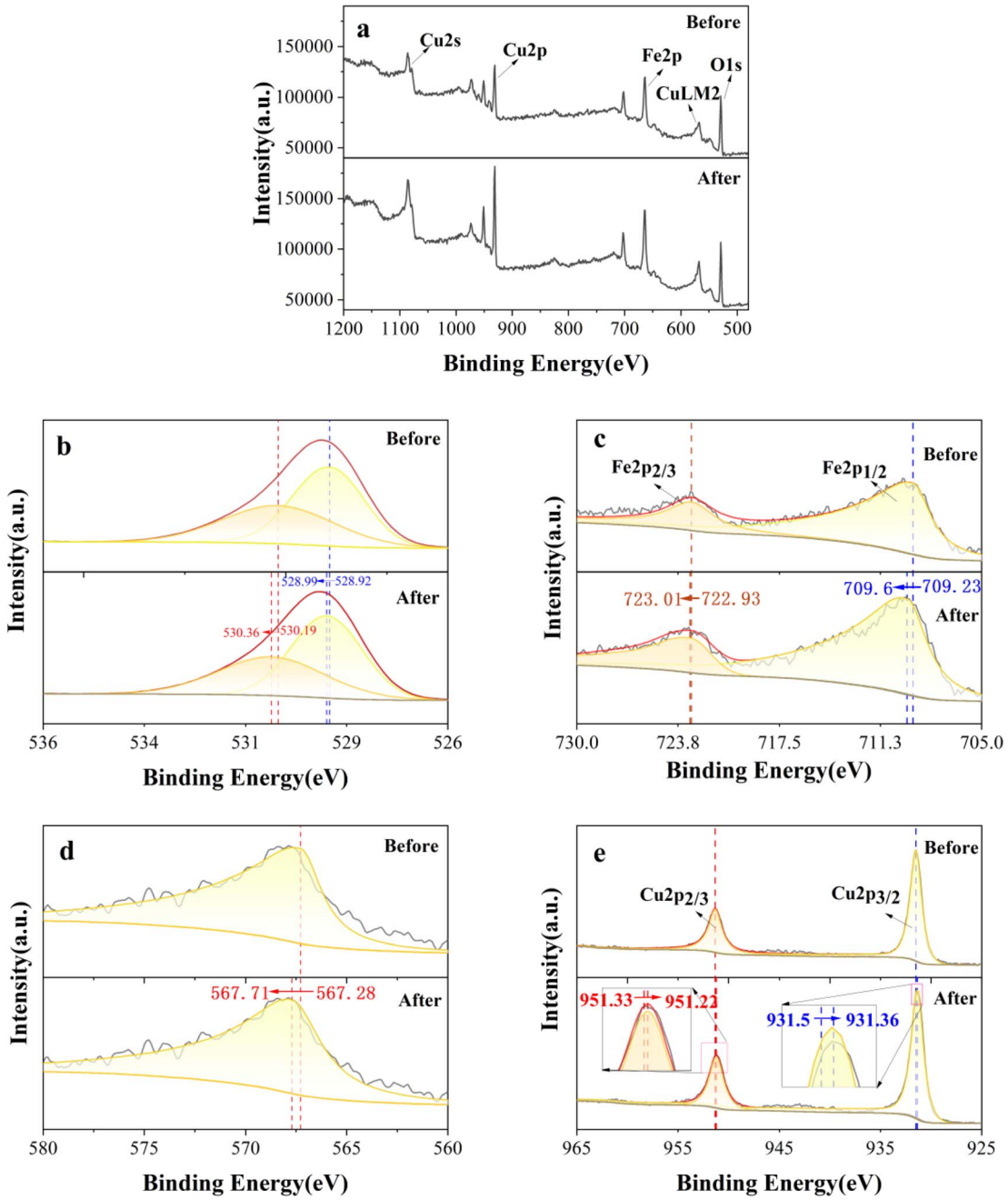

Fig. 9 (a) *In situ* XPS full spectrum image; (b) O1s spectrum image; (c) Fe2p spectrum image; (d) CuLM2 spectrum image; (e) Cu2p spectrum image.

mechanism follows an S-type mechanism. As a result, rapid recombination of weak charge carriers occurs, effectively preserving the potent h^+ and e^- in the VB of Fe_3O_4 and e^- in the VB of Fe_3O_4 and CB of Cu_2O.[25,26]

Under illumination, PDS undergoes activation, generating sulfate radicals ($SO_4^{\bullet-}$) directly, and can also be further activated by acquiring free electrons. During this process, photogenerated electrons facilitate the *in situ* redox cycling of Cu(II)/Cu(I) in $Cu_2O@Fe_3O_4$, significantly enhancing the activation efficiency of PDS and yielding more sulfate radicals ($SO_4^{\bullet-}$). These radicals may partially convert to $\cdot OH$ and $\cdot O_2^-$ during the reaction, subsequently combining with water molecules or dissolved oxygen to form species with potent oxidizing ability.

Furthermore, when free photo-excited electrons react with dissolved oxygen (DO) molecules, $\cdot OH$ and $\cdot O_2^-$ radicals are also generated. These radicals play a crucial role in degrading organic pollutants. Simultaneously, photogenerated holes directly participate in the decomposition of TC, accelerating the separation of electrons and holes, thereby enhancing the overall photocatalytic efficiency.

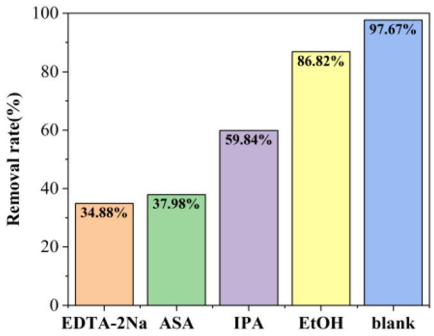

Fig. 10 Degradation of TC by $Cu_2O@Fe_3O_4$ composite catalyst in different free radical scavengers.

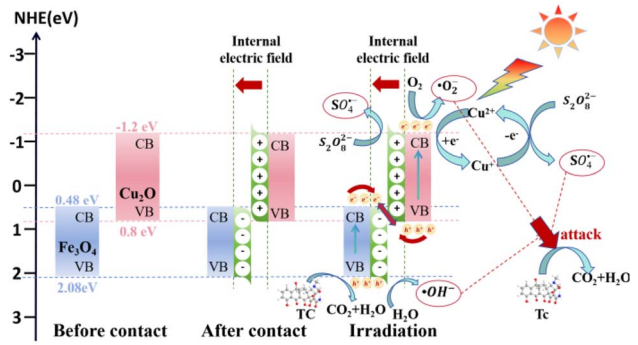

Fig. 11 $Cu_2O@Fe_3O_4$ mechanism of removal of TC by photocatalytic activation of PDS.

Conclusion

This study reports the preparation of a magnetic S-type heterojunction photocatalyst, $Cu_2O@Fe_3O_4$, *via* a simple hydrothermal method. Characterization through XRD, SEM, and EDS confirmed the successful synthesis of the $Cu_2O@Fe_3O_4$ composite material. Magnetic measurements revealed significant magnetic hysteresis behavior in $Cu_2O@Fe_3O_4$, indicating strong magnetic responsiveness and facilitating effective separation, recycling, and reuse of the composite material. UV-Vis spectroscopy experiments demonstrated superior light absorption performance of $Cu_2O@Fe_3O_4$ compared to pure Fe_3O_4 in the 300–500 nm spectral range. This composite material's estimated band gap was 1.74 eV, lower than the 2.12 eV of Fe_3O_4. This reduction in band gap widened the light absorption range, enhancing light absorption and the generation of photogenerated charge carriers, thereby improving the photocatalytic activity under visible light irradiation. The construction of the S-type heterojunction enabled efficient charge separation and optimal photo-redox power, leading to enhanced generation of active substances and improved photocatalytic performance of $Cu_2O@Fe_3O_4$.

The $Cu_2O@Fe_3O_4$ sample demonstrates remarkable photocatalytic efficiency in the PDS activation system. Under the conditions of pH 9, composite material concentration of 60 mg L^{-1}, and PDS concentration of 25 mg L^{-1}, 97.67% of TC is removed within 30 min. The degradation efficiency remains consistent even after five rounds of recycling, showcasing the excellent recyclability of $Cu_2O@Fe_3O_4$. Free radical trapping experiments revealed that the active radical species responsible for TC removal include h^+, $\cdot O_2^-$, $SO_4^{\bullet -}$ and $\cdot OH$.

Data availability

The authors confirm that the data supporting the findings of this study are available within the article.

Conflicts of interest

There are no conflicts to declare.

Acknowledgements

This research was funded by the Basic Scientific Research Youth Program (JYTQN2023373) of the Education Department of Liaoning Province and Muyuan Laboratory Research Program (14116022402, 14116022401).

References

1 Q. Chang, W. Wang, G. Regev-Yochay, M. Lipsitch and W. P. Hanage, Antibiotics in agriculture and the risk to human health: how worried should we be?, *Evol. Appl.*, 2014, **8**, 240–247, DOI: 10.1111/eva.12185.

2 F. Granados-Chinchilla and C. Rodríguez, Tetracyclines in Food and Feedingstuffs: From Regulation to Analytical Methods, Bacterial Resistance, and Environmental and Health Implications, *J. Anal. Methods Chem.*, 2017, **2017**, 1–24, DOI: 10.1155/2017/1315497.

3 Y. Leng, H. Xiao, Z. Li and J. Wang, Tetracyclines, sulfonamides and quinolones and their corresponding resistance genes in coastal areas of Beibu Gulf, China, *Sci. Total Environ.*, 2020, **714**, 136899, DOI: 10.1016/j.scitotenv.2020.136899.

4 Y. Gao, Q. Wang, G. Ji and A. Li, Degradation of antibiotic pollutants by persulfate activated with various carbon materials, *Chem. Eng. J.*, 2022, **429**, 132387, DOI: 10.1016/j.cej.2021.132387.

5 Z.-Y. Lu, Y. Ma, J. Zhang, N.-S. Fan, B.-C. Huang and R.-C. Jin, A critical review of antibiotic removal strategies: performance and mechanisms, *Journal of Water Process Engineering*, 2020, **38**, 101681, DOI: 10.1016/j.jwpe.2020.101681.

6 M. Priyadarshini, I. Das, M. M. Ghangrekar and L. Blaney, Advanced oxidation processes: performance, advantages, and scale-up of emerging technologies, *J. Environ. Manage.*, 2022, **316**, 115295, DOI: 10.1016/j.jenvman.2022.115295.

7 G. Chen, Y. Yu, L. Liang, X. Duan, R. Li, X. Lu, B. Yan, N. Li and S. Wang, Remediation of antibiotic wastewater by coupled photocatalytic and persulfate oxidation system: a critical review, *J. Hazard. Mater.*, 2021, **408**, 124461, DOI: 10.1016/j.jhazmat.2020.124461.

8 Y. Zhao, Y. Hu, H. Hao, F. Zhu, G. Zhang, J. Bi, S. Yan and H. Hou, Construction of an S-Scheme $Ag_2MoO_4/ZnFe_2O_4$ Nanofiber Heterojunction for Enhanced Photoelectrocatalytic Activity under Visible Light Irradiation, *Langmuir*, 2022, **38**, 13437–13447, DOI: **10.1021/acs.langmuir.2c01881**.

9 Z. Wang, Z. Lin, S. Shen, W. Zhong and S. Cao, Advances in designing heterojunction photocatalytic materials, *Chin. J. Catal.*, 2021, **42**, 710–730, DOI: **10.1016/s1872-2067(20)63698-1**.

10 Q. Wang, Y. Yang, S. Ma, J. Wu and T. Yao, Preparation of Fe_3O_4@Prussian blue core/shell composites for enhanced photo-Fenton degradation of rhodamine B, *Colloids Surf., A*, 2020, **606**, 125416, DOI: **10.1016/j.colsurfa.2020.125416**.

11 Z. Kuspanov, B. Baglan, A. Baimenov, A. Issadykov, M. Yeleuov and C. Daulbayev, Photocatalysts for a sustainable future: innovations in large-scale environmental and energy applications, *Sci. Total Environ.*, 2023, **885**, 163914, DOI: **10.1016/j.scitotenv.2023.163914**.

12 S. Li, C.-C. Wang, M. Cai, F. Yang, Y. Liu, J. Chen, P. Zhang, X. Li and X. Chen, Facile fabrication of $TaON/Bi_2MoO_6$ core–shell S-scheme heterojunction nanofibers for boosting visible-light catalytic levofloxacin degradation and Cr(VI) reduction, *Chem. Eng. J.*, 2022, **428**, 131158, DOI: **10.1016/j.cej.2021.131158**.

13 X. Li, Q. Luo, L. Han, F. Deng, Y. Yang and F. Dong, Enhanced photocatalytic degradation and H_2 evolution performance of N CDs/S-C_3N_4 S-scheme heterojunction constructed by π-π conjugate self-assembly, *J. Mater. Sci. Technol.*, 2022, **114**, 222–232, DOI: **10.1016/j.jmst.2021.10.030**.

14 D. Jiang, J. Xue, L. Wu, W. Zhou, Y. Zhang and X. Li, Photocatalytic performance enhancement of CuO/Cu_2O heterostructures for photodegradation of organic dyes: effects of CuO morphology, *Appl. Catal., B*, 2017, **211**, 199–204, DOI: **10.1016/j.apcatb.2017.04.034**.

15 L. Wan, Q. Zhou, X. Wang, T. E. Wood, L. Wang, P. N. Duchesne, J. Guo, X. Yan, M. Xia, Y. F. Li, A. A. Jelle, U. Ulmer, J. Jia, L. Tian, W. Sun and G. A. Ozin, Cu_2O nanocubes with mixed oxidation-state facets for (photo) catalytic hydrogenation of carbon dioxide, *Nat. Catal.*, 2019, **2**, 889–898, DOI: **10.1038/s41929-019-0338-z**.

16 M. Liu, Y. Ye, J. Ye, T. Gao, D. Wang, G. Chen and Z. Song, Recent Advances of Magnetite (Fe_3O_4)-Based Magnetic Materials in Catalytic Applications, *Magnetochemistry*, 2023, **9**, 110, DOI: **10.3390/magnetochemistry9040110**.

17 K. Li, M. Chen, L. Chen, S. Zhao, W. Xue and Y. Han, Synthesis and Application of a Fe_3O_4/Ag_3PO_4/g-C_3N_4 Magnetic Composite Photocatalyst for Sulfonamide Antibiotics Degradation, *Sustainability*, 2023, **15**, 13279, DOI: **10.3390/su151713279**.

18 G. G. Welegergs, H. G. Gebretinsae, M. G. Tsegay, C. Mtshali, N. Mongwaketsia, K. Cloete, Z. Y. Nuru, S. Dube and M. Maaza, Single-Layered Biosynthesized Copper Oxide (CuO) Nanocoatings as Solar-Selective Absorber, *Appl. Sci.*, 2023, **13**, 1867, DOI: **10.3390/app13031867**.

19 C. Shan, Z. Su, Z. Liu, R. Xu, J. Wen, G. Hu, T. Tang, Z. Fang, L. Jiang and M. Li, One-Step Synthesis of Ag_2O/Fe_3O_4 Magnetic Photocatalyst for Efficient Organic Pollutant Removal via Wide-Spectral-Response Photocatalysis–Fenton Coupling, *Molecules*, 2023, **28**, 4155, DOI: **10.3390/molecules28104155**.

20 J. Xu, J. Shen, H. Jiang, X. Yu, W. A. Qureshi, C. Maouche, J. Gao, J. Yang and Q. Liu, Progress and challenges in full spectrum photocatalysts: mechanism and photocatalytic applications, *J. Ind. Eng. Chem.*, 2023, **119**, 112–129, DOI: **10.1016/j.jiec.2022.11.057**.

21 M. M. Sajid, T. Alomayri, H. Zhai and A. A. Kareem, Construction of novel an in-situ m-$BiVO_4$/t-$BiVO_4$ isotype heterojunction photocatalyst for improved visible light-dependent degradation of dye, *Inorg. Chem. Commun.*, 2023, **157**, 111335, DOI: **10.1016/j.inoche.2023.111335**.

22 B. Xia, B. He, J. Zhang, L. Li, Y. Zhang, J. Yu, J. Ran and S. Qiao, $TiO_2/FePS_3$ S-Scheme Heterojunction for Greatly Raised Photocatalytic Hydrogen Evolution, *Adv. Energy Mater.*, 2022, **12**, 2201449, DOI: **10.1002/aenm.202201449**.

23 J. Wang, X. Qiao, W. Shi, J. He, J. Chen and W. Zhang, S-Scheme Heterojunction of Cu_2O Polytope-Modified BiOI Sheet for Efficient Visible-Light-Driven CO_2 Conversion under Water Vapor, *Acta Phys.-Chim. Sin.*, 2022, 2210003, DOI: **10.3866/pku.whxb202210003**.

24 G. U. Rehman, M. Tahir, P. S. Goh, A. F. Ismail and I. U. Khan, Controlled synthesis of reduced graphene oxide supported magnetically separable Fe_3O_4@rGO@AgI ternary nanocomposite for enhanced photocatalytic degradation of phenol, *Powder Technol.*, 2019, **356**, 547–558, DOI: **10.1016/j.powtec.2019.08.026**.

25 S. Li, M. Cai, Y. Liu, C. Wang, K. Lv and X. Chen, S-Scheme photocatalyst $TaON/Bi_2WO_6$ nanofibers with oxygen vacancies for efficient abatement of antibiotics and Cr(VI): intermediate eco-toxicity analysis and mechanistic insights, *Chin. J. Catal.*, 2022, **43**, 2652–2664, DOI: **10.1016/s1872-2067(22)64106-8**.

26 Q. Xu, L. Zhang, B. Cheng, J. Fan and J. Yu, S-Scheme Heterojunction Photocatalyst, *Chem*, 2020, **6**, 1543–1559, DOI: **10.1016/j.chempr.2020.06.010**.